Research Article

Determination of Anisotropic Mechanical Properties for Materials Processed by Laser Powder Bed Fusion

Even W. Hovig ⬡,[1] **Amin S. Azar** ⬡,[2] **Frode Grytten** ⬡,[2] **Knut Sørby** ⬡,[1] **and Erik Andreassen** ⬡[2]

[1]*Norwegian University of Science and Technology (NTNU), Department of Production and Quality Engineering, Trondheim, Norway*
[2]*SINTEF Industry, Oslo, Norway*

Correspondence should be addressed to Even W. Hovig; even.w.hovig@ntnu.no

Improving the success rate in additive manufacturing and designing highly optimized structures require proper understanding of material behaviour. This study proposes a novel experimental method by which anisotropic mechanical properties of additively manufactured materials can be assessed. The procedure is based on tensile testing of flat specimens, manufactured by laser powder bed fusion (LPBF) at different orientations relative to the build plate. In this study, the procedure was applied to the Inconel 718 alloy. Three identical specimen sets were built, each of which received complementary postprocessing treatments. The tensile tests were carried out on specimens with as-built surface finish. Digital image correlation was used to record the strain field evolution on two perpendicular surfaces of the tensile specimens under loading. An optimization algorithm is also proposed for determining the anisotropic elastic constants using only a few tensile test results. It was observed that both build orientation and postprocessing have strong influence on the anisotropic mechanical properties of the material. The effect of microstructure was also investigated and characterised. Consequently, three transversely isotropic compliance matrices were constructed, representing the effect of the different processing conditions.

1. Introduction

Most of the commercial additive manufacturing (AM) technologies can produce materials with relatively high density and decent mechanical properties, close to that of classical processing methods. Capability of manufacturing complex geometries by AM brought about new opportunities such as "topology optimization" and "design for additive manufacturing (DfAM)" and caused commencement of a new chapter in performance-oriented design of components. Several challenges, such as anisotropic behaviour [1–6] and effects of postprocessing steps [7–10], need to be addressed in the design phase to release the full potential of AM. Despite these facts, most of the current algorithms for

generative design use isotropic material models or globally uniform and defect-free properties [11–13]. Thus, we propose a methodology for calibrating anisotropic constitutive material models based on systematic mechanical tests and as-built surface conditions. Inconel 718 (IN718) processed by laser powder bed fusion (LPBF) are the material and process of choice in this study.

1.1. Determination of Elastic Constants—Transversely Isotropic Elastic Materials. Anisotropic elasticity can be modelled using the generalized Hooke's law. If the material is assumed to be transversely isotropic, that is, isotropic in the XY plane, Hooke's law can be expressed as [14]

$$
\begin{bmatrix} \varepsilon_{xx} \\ \varepsilon_{yy} \\ \varepsilon_{zz} \\ \varepsilon_{yz} \\ \varepsilon_{xz} \\ \varepsilon_{xy} \end{bmatrix} = \begin{bmatrix} \dfrac{1}{E_{xx}} & -\dfrac{\nu_{xy}}{E_{xx}} & -\dfrac{\nu_{zx}}{E_{zz}} & 0 & 0 & 0 \\[2mm] -\dfrac{\nu_{xy}}{E_{xx}} & \dfrac{1}{E_{xx}} & -\dfrac{\nu_{zx}}{E_{zz}} & 0 & 0 & 0 \\[2mm] -\dfrac{\nu_{xz}}{E_{xx}} & -\dfrac{\nu_{xz}}{E_{xx}} & \dfrac{1}{E_{zz}} & 0 & 0 & 0 \\[2mm] 0 & 0 & 0 & \dfrac{1}{2G_{xz}} & 0 & 0 \\[2mm] 0 & 0 & 0 & 0 & \dfrac{1}{2G_{xz}} & 0 \\[2mm] 0 & 0 & 0 & 0 & 0 & \dfrac{1}{2G_{xy}} \end{bmatrix} \begin{bmatrix} \sigma_{xx} \\ \sigma_{yy} \\ \sigma_{zz} \\ \sigma_{yz} \\ \sigma_{xz} \\ \sigma_{xy} \end{bmatrix}.
\tag{1}
$$

The E_{xx} and E_{zz} moduli can be found using standard tensile tests. The shear modulus in the plane of isotropy can be expressed as [14]

$$
G_{xy} = \frac{E_{xx}}{2(1 + \nu_{xy})}.
\tag{2}
$$

G_{xz} can be calculated using an off-axis tension test to determine E_ϕ on a sample built in the XZ plane with a rotation of $\phi = 45°$ about the Y-axis. This E_ϕ, assuming negligible shear strain, can then be used to calculate G_{xz}, using the following equation [15]:

$$
G_{12} = \frac{\sin^2 \phi \cos^2 \phi}{(1/E_\phi) - (\cos^4 \phi/E_1) - (\sin^4 \phi/E_2) + ((\nu_{21}/E_1) + (\nu_{12}/E_2))\sin^2 \phi \cos^2 \phi},
\tag{3}
$$

where the principal directions 1 and 2 correspond to Y and Z, respectively, and E_ϕ is the measured elastic modulus in the off-axis tension test. Note that E_ϕ can only be determined using the off-axis tension test if the following inequality is satisfied [15]:

$$
G_{12} \geq \frac{E_1}{2(1 + \nu_{21})}.
\tag{4}
$$

Another approach to determine the elastic constants is to implement the problem as an optimization problem by minimizing a function of several variables and constraints. A proposed solution for this is presented in Section 2.4.

1.2. Inconel 718. IN718 was developed in an effort to improve weldability and strain-aged cracking resistance. It is a hardenable alloy of Ni-Fe-Cr, which takes advantage of $Ni_3[Al,Ti]$ (γ' phase, fcc) and Ni_3Nb (γ'' phase, bct) precipitates to increase the resistance to cracking because of slow formation kinetics of these constituents. This alloy is known to have excellent corrosion and fatigue properties at service temperatures up to 760°C [16]. Typical IN718 compositions for wrought and powder material are given in Table 1.

The precipitates are mostly coherent with the austenite matrix that increases the mechanical strength of the material by co-straining with the matrix under different loading conditions. However, some precipitates can adversely affect the performance of these alloys, especially when they are exposed to high temperatures for a relatively long period of time [18]. Figure 1 shows the calculated and experimentally determined TTT diagrams for IN718 that will be used to determine the heat treatment cycle later in this work. The formation kinetics and thermodynamics of

γ' and γ'' precipitates are analogous in these diagrams; γ' forms at a slightly higher temperature range, which is indicative of the importance of accurate temperature control in the ageing process. Despite that both the calculated and experimentally determined TTT curves are addressing the nominal IN718 material, slight variation in the chemical composition may result in discrepancy between the two approaches when exact formation kinetics of the γ' and γ'' are being investigated. In addition to solid solution strengthening, the strength can be obtained through formation of γ'' phase in this alloy. The γ' phase is brittle, and its formation is less preferred to increase the high and low temperature ductility. Other brittle phases such as δ may also form upon long exposure to elevated temperatures. Therefore, the service temperature of this alloy is limited by the formation of δ and σ phases.

1.3. Additive Manufacturing of Inconel 718. In laser powder bed fusion (LPBF), the starting point is a packed bed of powder material—usually prealloyed—that is fused locally using an adjustable laser heat source. Today's advanced machines spread the powder in layer thicknesses ranging from 30 to 200μm [21, 22]. Selection of layer thickness is a trade-off between build rate and part quality, and the chosen layer thickness is a breakeven point for achieving the best built rate with satisfactory quality [23, 24].

There are several features that can cause anisotropy in AM materials. Porosity and pore shape [25], microstructure and texture [26–29], and surface finish [30, 31] of the AM material are among the most referred reasons for anisotropic behaviour. Previous studies have captured the anisotropic properties of various heat treatments of laser powder bed

TABLE 1: Chemical composition of a commercial wrought solution-treated IN718 [17] and the commercial IN718 powder used in this study (specifications from the supplier).

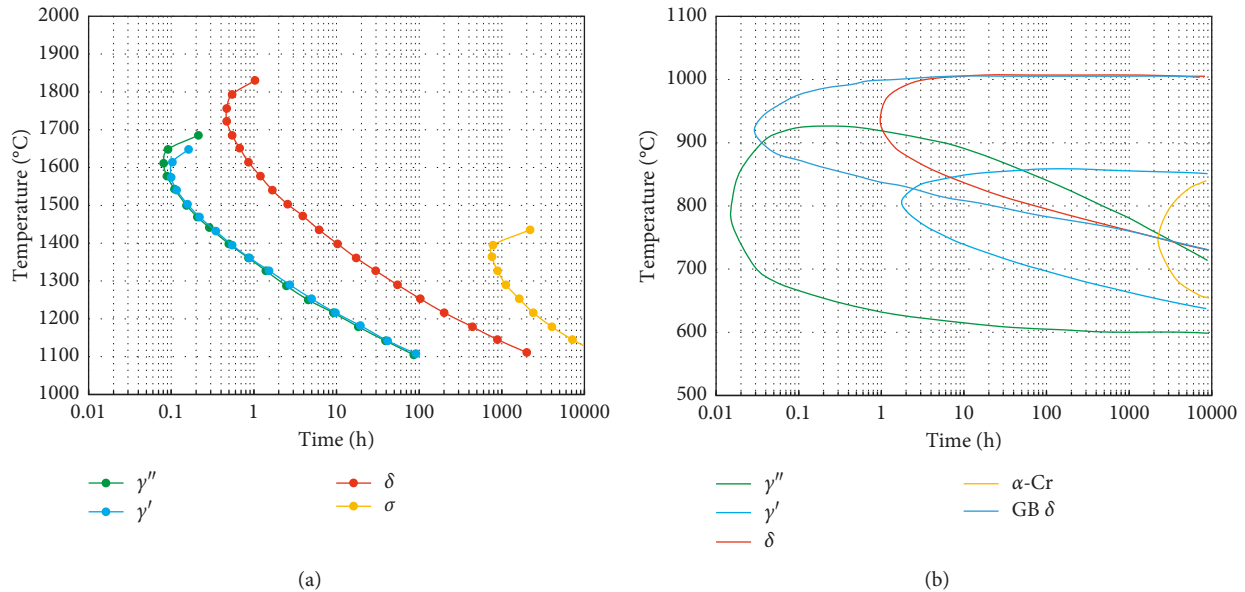| Element	Ni	Cr	Fe	Al	Mo	Nb (+Ta)	Ti
wt.%, commercial wrought	53	19	18.5	0.5	3.0	5.1	0.9
wt.%, commercial powder	50–55	17–21	Bal.	0.2–0.8	2.8–3.3	4.75–5.5	0.6–1.1

(a)

(b)

FIGURE 1: TTT diagram for IN718, calculated (a) and experimentally determined (b) [19, 20].

fusion Inconel 718 [11, 32–34]. The mentioned studies were not focused on determining anisotropic elastic properties, and thus excluded required orientations and mechanical properties (i.e., Poisson's ratio).

Since the powder bed surface is always set horizontally and parallel to the build plate, placement of the components at different angles will result in various grain growth orientations with reference to the local coordinate system of the component. Therefore, applying the same process parameters, including the laser scanning strategy, will cause evolution of disparate crystallographic textures depending on the build orientation [35]. Disregarding surface effects, this phenomenon is the major source of anisotropic behaviour in the same material that is processed at different build orientations. Figure 2 compares two possible grain growth directions induced by varied build parameters. These grains are assumed to undergo a biaxial loading in the presented direction annotated with F. It was also assumed that the grains are at one side of the melt pool and there is a symmetry in the growth shown by centreline annotation C_L. Moreover, the local coordinate system at each arbitrary location along the grain is indicated on the cross-cutting plane with <100> orientation as the normal vector. Figure 2 (a) schematically shows a slow cooling rate and Figure 2(b) presents a higher cooling rate. The latter is the dominant case in LPBF. After solidification, two differently oriented grains will be loaded along a certain crystal orientation. Therefore,

the mechanical response of the material would apparently differ if identical parts are produced with various relative orientations to the build plate.

Choi et al. [36], Wang et al. [37], and Keshavarzkermani et al. [38] are among the researchers who investigated the microstructure and texture of IN718, processed by LPBF. In all these studies, the matrix mainly consists of γ grains. The grains were oriented nearly in the same direction, almost like a single crystal. According to their reported electron backscatter diffraction (EBSD) analysis, the γ matrix grains were oriented with <100> parallel to the build direction. Azar et al. [39] showed that the cubic crystal growth along <100> follows the maximum heat flow direction in welding, which is perpendicular to the powder layers in the LPBF case. According to Azar et al. [39], depending on the heat source dynamics and solidification kinetics, the crystals can follow a curvilinear path where the <100> is rotating (Figure 2).

Murr et al. [40, 41] reported that HIP treating the IN718 alloy increases the ductility of the material significantly, which is related to reduction in the residual stresses and hardness of the precipitates. Wang et al. [42] summarised the heat treatment cycles that were applied by previous researchers for IN718 processed by AM. The major driving force for optimising the heat treatment procedure is to maximise the evolution of advantageous phases while suppressing the formation of the detrimental ones.
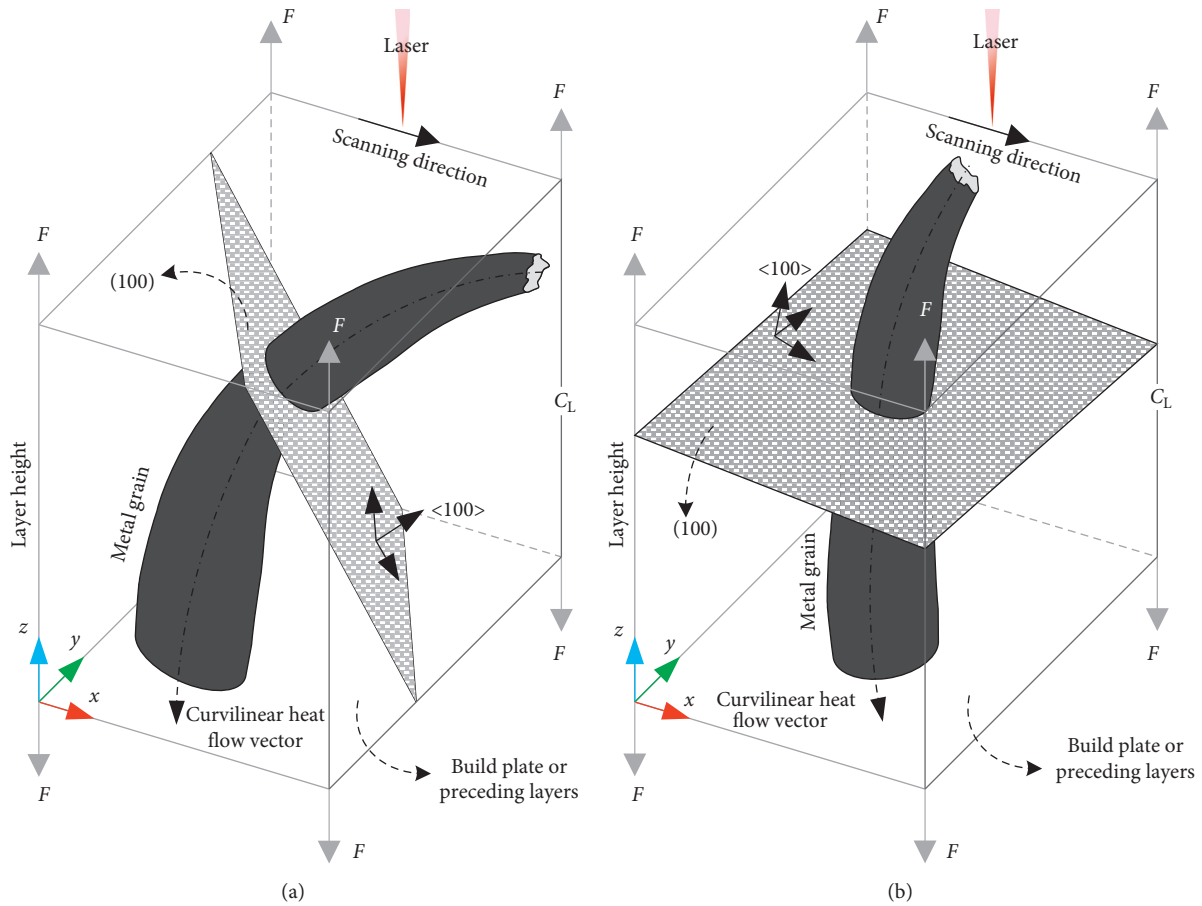
FIGURE 2: Differences in growth kinetics of metal grains along maximum heat flow. This schematic illustration shows two different grain positions with respect to the future loading conditions. In (a), the loading is close to the crystallographic <111> while in (b), the loading is close to <100>.

2. Materials and Methods

In order to investigate the anisotropy of the additively manufactured IN718 material, the tensile specimens were manufactured at various orientations with respect to the horizontal build plate. In this section, the entire chain from powder to postprocessing, and testing will be summarised.

2.1. IN718 Powder. Prior to the LPBF processing, the powder morphology and chemistry were investigated. The powder used was from a recycled batch, which was sieved and dehumidified following standard practices. The morphology of the powder particles was determined using a Malvern G3 Morphology instrument in the dry dispersion mode. The powder was dispersed on a microscope slide and particles were captured for analysis one-by-one. About 33,000 particles were scanned in the analysis. The chemical composition of the powder was determined by energy-dispersive X-ray spectroscopy (EDS) mapping in a scanning electron microscope (SEM).

2.2. Laser Parameters and Sample Preparation. The tensile samples were built in an LPBF machine (SLM 280 HL from SLM Solutions, installed 2014), with process parameters for IN718 powder as supplied by SLM Solutions [43]. The main process parameters are given in Table 2.

The density of the specimen is related to the energy in the LPBF process [44], with the energy per area ($J \cdot m^{-2}$) defined as $E_A = P/vd$, where P is the laser power (W), v is the scanning velocity ($m \cdot s^{-1}$), and d is the hatch spacing (m). In this study, the energy density formula will be used to benchmark the build conditions against earlier published data. The relative density of the material was calculated on polished cross sections of the material using optical microscopy and an image-processing approach (ImageJ software).

Flat tensile specimens were produced in three sets, each consisting of 11 specimens built at different orientations. The sample orientation with respect to the build plate starts at horizontal (0°) increasing to vertical (90°) with 15° increments. Figure 3 shows the tensile specimen geometry, and Figure 4 shows the 11 specimen orientations for each set. The sample geometry and dimensions were initially designed for in situ tensile tests in an SEM, which is the subsequent study of this work. The colours correspond to the orientations in Table 3. The tensile specimens were not machined after LPBF, as the goal of the study is to assess

TABLE 2: Process parameters.

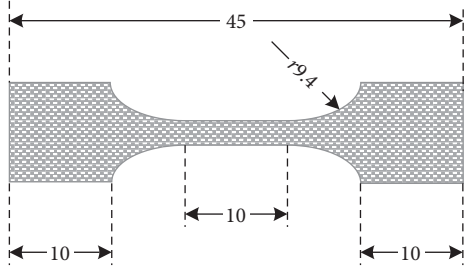| Laser power, P (W)	Layer thickness, t (μm)	Hatch spacing, d (μm)	Scan velocity, v (mm/s)
275	50	120	805

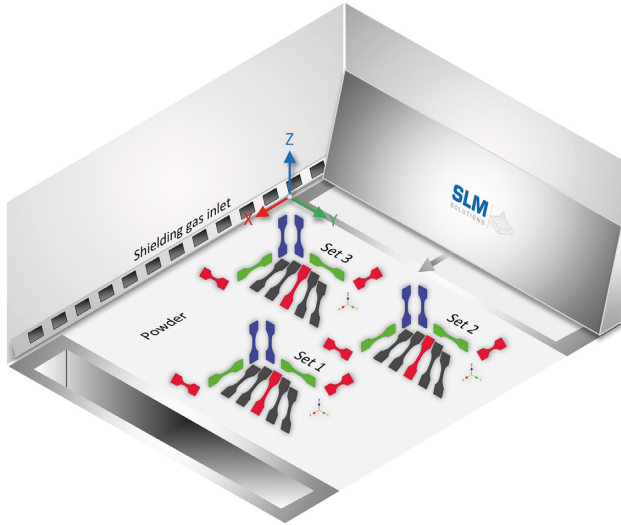FIGURE 3: Geometry of the tensile specimen. Dimensions are in mm.

FIGURE 4: Orientation of the specimens and their configuration in the LPBF build platform. The colours indicate the samples that are used for determining the elastic constants in Section 2.3. Orientations are according to Table 3.

TABLE 3: Codes for test specimen orientation corresponding to Figure 4, with similar choice of colours. Orientation annotation is according to ISO/ASTM 52921:2013E.

ZX	ZY		
XZ	YZ		
XZ − 45B	XY + 45B	YZ + 45A	
XY + 15B	XY + 30B	XY + 60B	XY + 75B

and classify the behaviour of LPBF components with as-built surfaces. In addition to the LPBF specimens, some reference specimens were machined from rolled and aged IN718.

Three different postprocessing routes (denoted as "sets") were designed. Each route was applied to a complete set of sample orientations. Tables 4–6 summarise the applied postprocessing parameters based on the instructions found in reference [45]. (S), (A), and (H) abbreviations were used to show the postprocessing steps of solution treatment, ageing, and HIP, respectively. The solution treatment was performed prior to the removal of the specimens from the build plate. HIP was performed by Bodycote AB.

2.3. Determination of Elastic Constants Using Digital Image Correlation. Using Digital Image Correlation (DIC) in combination with tensile testing [46] eliminates the need for strain gauges. It is sufficient to test at three orientations to determine the transversely isotropic compliance matrix. However, as shown in this study, it is necessary to increase the number of orientations to capture the mechanical response of the material. There are other methods available to capture anisotropy, such as magnetic resonance elastography [47] and nanoindentation [48]. However, these methods are dependent on the local properties of the materials and will only characterize the superficial surface layers.

A commercial DIC system (Vic3D) was used to determine the displacement fields during the tensile tests. The tensile tests were carried out using a Zwick tensile machine equipped with a 50-kN load cell. The cross-head speed was set to 1 mm/min. The cross-sectional area of each specimen was measured with a digital calliper and cross-checked with DIC to account for any deviation from the nominal dimensions. In addition, the surface roughness was measured with white light interferometry (WLI) to quantify the uncertainty of the measured cross-sectional area. Two cameras (2452 × 2052 pixels) equipped with Pentax 75 mm f/2.8 lenses were used. The cameras were mounted on a tripod such that two faces of the tensile sample were exposed to both cameras. This setup allows for the capture of out-of-plane displacements and in-plane displacements on the specimen surface. The correlation was performed with a subset of 29 pixels and a step size of 5 pixels. For a detailed description of the DIC setup, the reader is referred to reference [46].

The Lagrange strain was calculated using the Vic3D software, and the average principal and shear strains were exported for further processing in Matlab. For uniaxial loading of a specimen with gauge length L_0, the Lagrange strain can be written as

$$\varepsilon = \frac{\Delta L}{L_0} + \frac{1}{2}\left(\frac{\Delta L}{L_0}\right)^2. \tag{5}$$

Taking into account that the cross-sectional area varying as a load is applied, and introducing w as the current width, w_0 as the initial width, and similarly for the thickness t, the stress can be expressed as

TABLE 4: Set 1: instructions for solution treatment (S).

HT#	Description	Conditions	Holding temperature	Holding time	Cooling
1	Homogenization and solution treatment	Argon atmosphere. Fast heating to the target temperature	980°C	1 hr	Air cool

TABLE 5: Set 2: instructions for treatment (S + A).

HT#	Description	Conditions	Holding temperature	Holding time	Cooling
1	Homogenization and solution treatment	Argon atmosphere. Fast heating to the target temperature	980°C	1 hr	Air cool
2	Ageing	Vacuum/argon atmosphere. Fast heating to the target temperature	720°C	8 hr	Furnace cool to 620°C within 2 hours
3	Ageing	Vacuum/argon atmosphere. Fast heating to the target temperature	620°C	8 hr	Air cool

TABLE 6: Set 3: instructions for treatment (S + H + A).

HT#	Description	Conditions	Holding temperature	Holding time	Cooling
1	Homogenization and solution treatment	Argon atmosphere. Fast heating to the target temperature	980°C	1 hr	Air cool
2	HIP	100 MPa	1160°C	4 hr	Air cool
3	Ageing	Vacuum/argon atmosphere. Fast heating to the target temperature	720°C	8 hr	Furnace cool to 620°C within 2 hours
4	Ageing	Vacuum/argon atmosphere. Fast heating to the target temperature	620°C	8 hr	Air cool

$$\sigma = \frac{F}{A_0} \frac{w_0 t_0}{wt} = \frac{F}{A_0} \frac{1}{\sqrt{1 + 2\left[\left((w-w_0)/w_0\right) + \left((1/2)\left((w-w_0)/w_0\right)^2\right)\right]} \sqrt{1 + 2\left[\left((t-t_0)/t_0\right) + \left((1/2)\left((t-t_0)/t_0\right)^2\right)\right]}}, \quad (6)$$

or, in terms of strain, where subscript a denotes the axial direction:

$$\sigma_a = \frac{F}{A_0\left(\sqrt{1 + 2\bar{\varepsilon}_w}\ \sqrt{1 + 2\bar{\varepsilon}_t}\right)}. \quad (7)$$

Here, σ_a is the Cauchy stress, F is the current force, A_0 is the initial specimen cross-sectional area, and $\bar{\varepsilon}_w$ and $\bar{\varepsilon}_t$ are the average Lagrange strains [46] in the transverse directions for all points in the current cross section of the two AOIs, respectively. Thereafter, the Cauchy stress was used to find Young's moduli of the specimen in the load direction according to ASTM E111. Poisson's ratios were determined according to ASTM E132. With all the calculated terms, the compliance matrix can be constructed for a transversely isotropic material based on Equation (1) with colour codes corresponding to the samples in Figure 4.

2.4. Determination of Elastic Constants with an Optimization Algorithm.
Determining anisotropic material data via direct measurements requires a large dataset to eliminate random errors in the measurements. To improve the significance of the measurements and reduce the number of test specimens,

an optimization algorithm is implemented. This algorithm determines the elastic constants as a complementary solution to direct measurement using DIC. As it will be shown in this article, the benefit of determining the elastic constants by such optimization is that the data will be less vulnerable to noise in the strain measurements, since the algorithm weighs all the stress-strain pairs equally.

In this study, a set of measured stresses and corresponding strains is known for the tensile specimens with respect to the principal material direction. An optimization algorithm was implemented to optimize the compliance matrix.

Consider the transversely isotropic case for which Hooke's law can be expressed as Equation (1). Each pair of strain and stress is related by the compliance matrix and a transformation matrix $\mathbf{K}$, as derived by e.g., pp. 54–55 in Ting [14]. Hooke's law transforms to $' = \mathbf{S}'\sigma'$, where $\sigma' = \mathbf{K}\sigma$, and $\mathbf{S}' = (\mathbf{K}^{-1})^T \mathbf{S}\mathbf{K}^{-1}$, which leads to $' = (\mathbf{K}^{-1})^T \mathbf{S}\mathbf{K}^{-1}\mathbf{K}\sigma = (\mathbf{K}^{-1})^T \mathbf{S}\sigma$. $\mathbf{S}'$ and $\mathbf{S}$ are the transformed and original compliance matrix.

In the current study the Lagrange strain tensor is measured directly using DIC. The shear stress and strain were found to be negligible, allowing the procedure

described in Equation (3) to be used to calculate the shear moduli. When a relationship between stress and strain is established, the strain tensor can be expressed as

$$* = \left(\mathbf{K}^{-1}\right)^{T}\mathbf{S}\mathbf{K}^{-1}\boldsymbol{\sigma}, \tag{8}$$

where $\boldsymbol{\sigma}$ is the Cauchy stress tensor from Equation (7). The objective of the optimization problem is to minimize a cost function $J(\theta)$. A common cost function for problems like this is the root-sum-of-squares function shown in the following equation:

$$J(\theta) = \sum_{i=1}^{m} \sqrt{2 - '^{2}}, \tag{9}$$

where is the measured strain in the elastic region. An optimization problem like this can be implemented by e.g., the function fmincon in Matlab. The material is assumed to increase in volume and contract in the transverse directions when undergoing tensile stress. This in turn constrains the Poisson's ratio in any orientation to be bound by $0 < \nu_{ij} < 0.5$. As the elastic moduli in the 0°, 45° and 90° orientations are known, the problem is reduced to determining the Poisson's ratios. The elastic moduli in the compliance matrix (Equation (1)) are known and are used together with the constraints on the Poisson's ratios to determine ν_{xy}, ν_{xz}, and ν_{zx}. The shear moduli are determined based on Equations (2) and (3).

2.5. Electron Microscopy and Electron Backscattered Diffraction (EBSD) Analysis.

In order to investigate the effect of postprocessing conditions on the grain structure using SEM, the samples were prepared by means of mechanical grinding and polishing followed by etching. Glyceregia solution was used for etching the samples. In the interest of studying crystallographic texture and preferred crystallographic orientations, EBSD analysis was employed. For this purpose, the 90° ZY specimens from set 1 and set 3 were selected. These samples were also prepared by mechanical grinding and polishing, though, instead of final etching, Oxide Polishing Suspension (OP-S, 0.04 μm) from Struers was applied. The EBSD sample was extracted from the side wall of this specimen. The backscattered patterns were collected in offline mode using FEI NOVA NANOSEM 650 ultralow vacuum field emission gun scanning electron microscope (SEM). An EBSD detector (Oxford Instruments NordlysMax3) was used to record approximately 1000 offline patterns per second. The working distance was set to 11 mm with a tilt angle of 70° under a high-current electron beam. The accelerating voltage of the gun was 20 kV. An area of 800 μm × 800 μm was scanned with step size 400 nm, accumulating crystallographic data for 4 million points for the selected area.

3. Results

3.1. Powder Characterization.

Figure 5 shows the statistical values for the particle analysis. The figure contains information about circle equivalent (CE) diameter, high sensitivity (HS) circularity, aspect ratio and elongation for the analysed
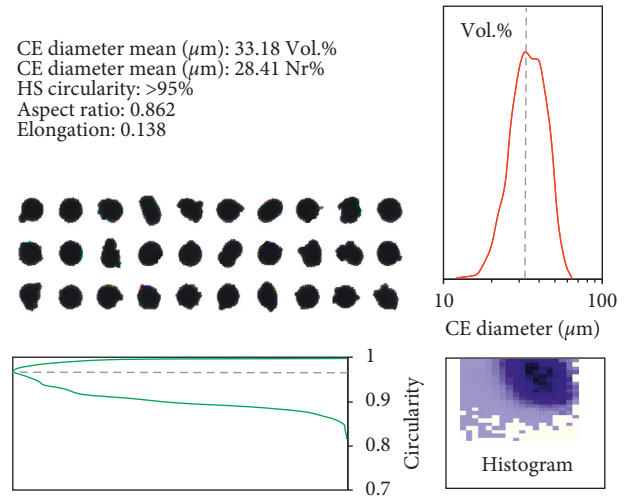

FIGURE 5: IN718 powder morphology analysis.

powder. Description of these entities is given in reference [49]. Moreover, selected individual particles in the vicinity of the peak of the distribution are shown in the figure. The vertical axis in the CE diameter figure is reported in arbitrary units (a.u.). The vertical and horizontal axes in the histogram figure are reflected in the upper and left figures in Figure 5.

Figure 6 shows the chemical composition mapping of the particles. Some particles are rich in Al-Co-Ni content and depleted in other elements. Although there are local inhomogeneities in the chemical composition of the particles, the mass composition of the powder is within the specifications of IN718 datasheet.

3.2. Microstructure.

Figure 7 shows SEM images of the XY + 45B tensile sample from set 1 at three locations. The observed steps are a result of the "stair-stepping" effect, and the distance between each step perpendicular to the page is the layer height. The edge steps were measured directly on the figure and the layer height was calculated based on the known nominal inclination (45°). The layer height was also checked and compared, both by focusing the scanning electron beam of the microscope on each two adjacent steps and measuring from the cross section. The results are tabulated in Table 7.

Figure 8 shows high-magnification SEM micrographs of a specimen from set 1. Figure 8(a) shows the fusion lines along the build direction, and Figure 8(b) shows the $\gamma + \gamma''$ lamellae structure at a higher magnification. White and blue arrows show some of the typical flaws in the matrix resulting from lack of fusion, and microsegregation in the interdendritic regions, respectively.

SEM micrographs of the aged specimens (SET 2) in Figure 9 show dendritic lamellae and grain boundary δ/η-phase evolution after ageing.

Figure 10(a) illustrates the acquisition conditions for the EBSD investigations. The build direction is along Y0 in the figure, leaving the LPBF layers perpendicular to Y0. Figure 10(b) presents the inverse pole figure Y0 (IPF-Y0) of the scanned area. In this frame, north of the figure is X0 and east
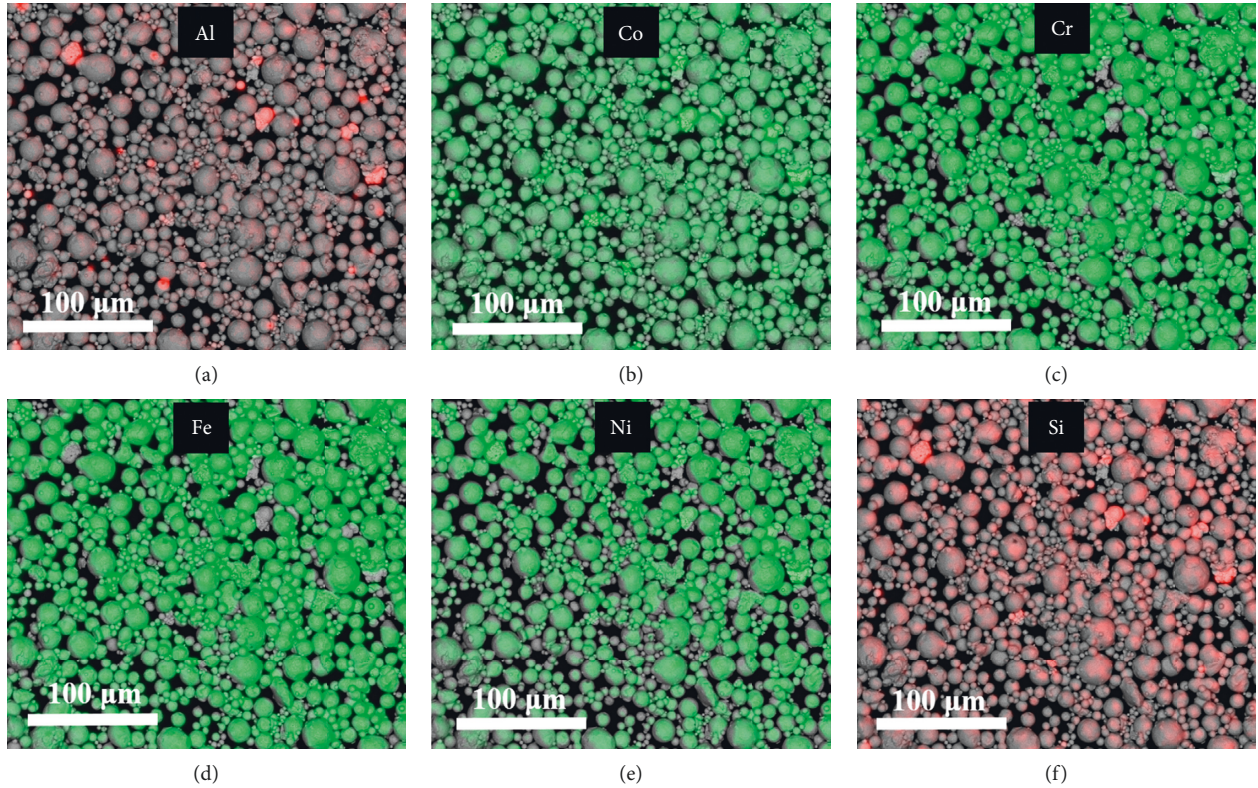
(a) (b) (c)

(d) (e) (f)

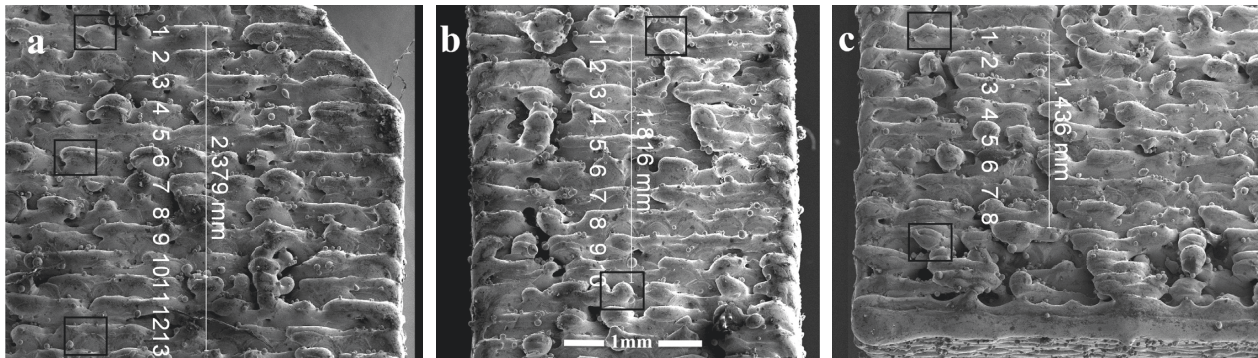Figure 6: EDS chemical composition mapping of the used IN718 powder.

Figure 7: Surface topography of the upwards facing surface of the $XY + 45B$ specimen from set 1 at the (a) top; (b) middle; and (c) bottom of the tensile sample.

Table 7: Layer and edge step measurements.

Site	Layers	Total width (μm)	Width of single layer (μm)	Layer height (μm)
a	13	2379	183.0	49.0
b	10	1816	181.6	48.7
c	8	1436	179.5	48.1

of the frame is $Y0$. The dataset was rotated 90° counter-clockwise to capture the texture of the material correctly.

Figures 11(a) and 11(b) show the inverse pole figures of the scanned area for samples from set 1 and set 3. It can be seen that the preferred orientation of {100}<100>||$Y0$ is dominating in set 1 as a result of the build conditions. In other words, the {100} family of planes is preferably oriented towards the build orientation if the sample is set at 90° with respect to the build platform. Traces of texture components in the samples from set 3 can still be seen. However, due to extensive recrystallization and ageing after postprocessing (HIPing + ageing), the texture is weakened. This can be observed by comparing the orientation clustering densities in the legend of both figures.

Figure 12 shows the orientation distribution function (ODF) space of the scanned area for the sample from set 1. The ideal texture component of <100>||$Y0$ was also plotted in each section. It is apparent that the hot spots on different sections of $\phi2$ Euler angle coincide well with the presented ideal orientation, suggesting that there is a dominating texture component in the specimen.
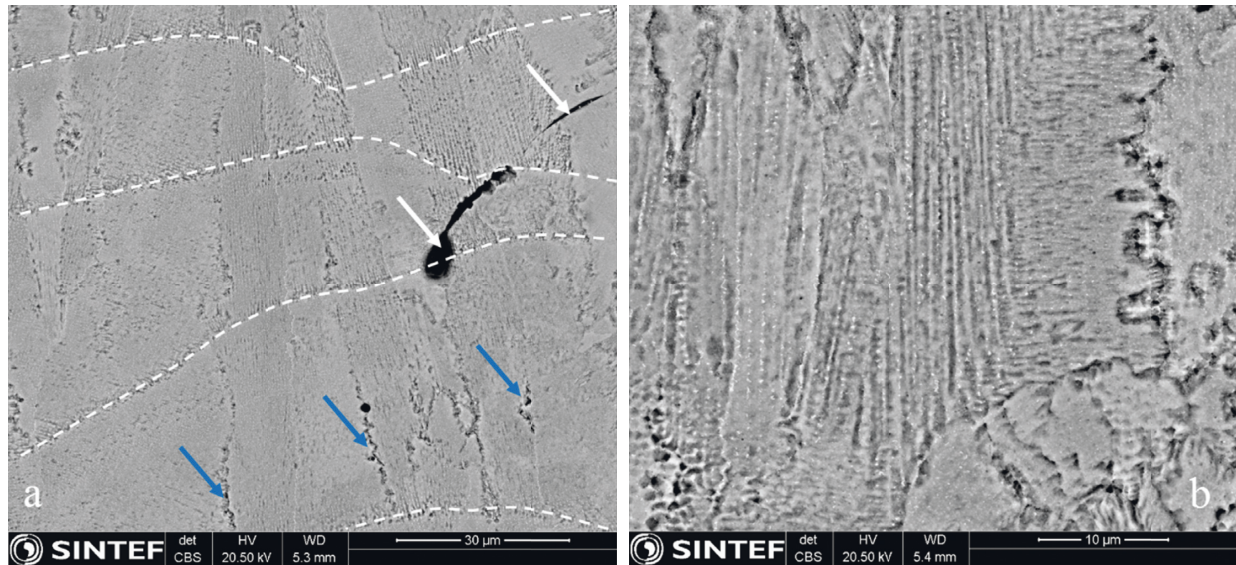
FIGURE 8: SEM micrographs from the solution-treated samples (Set 1) (a) showing the fusion lines, white arrows show the lack of fusion due to laser parameters and blue arrows show the inter-dendritic regions. (b) showing the dendritic $\gamma + \gamma''$ lamellae structure.
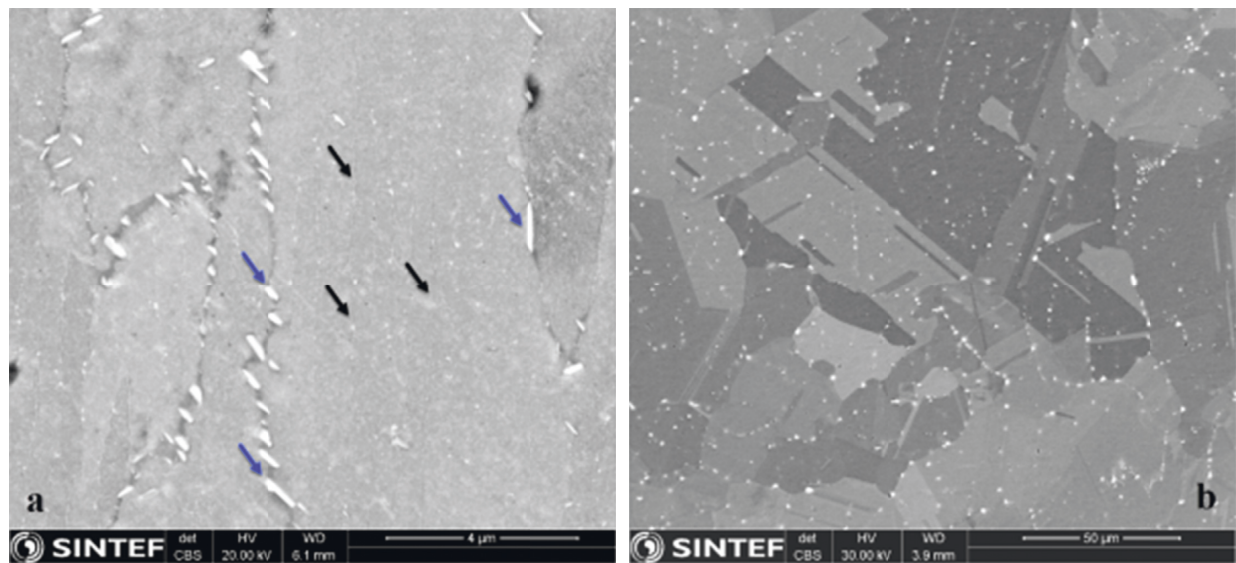

FIGURE 9: SEM micrograph of (a) aged IN718, and (b) HIPed and aged IN718. Black arrows show the interdendritic $\gamma + \gamma''$ lamellae, and blue arrows show the evolution of grain boundary δ/η-phase upon ageing. Extensive reconstructions of the grain structure, and grain boundary precipitates mostly on the prior boundaries of γ grains can be seen in (b).

3.3. Mechanical Properties. The relative density was measured to be 99.97% (set 1) and 99.98% (set 3). Figure 13 shows Cauchy stress versus Lagrange strain for set 1 (a), set 2 (b) and set 3 (c), with postprocessing as described in Tables 4–6, respectively.

Figure 14 shows the elastic modulus for set 1 (a), set 2 (b), and set 3 (c) for all build orientations. The error bars indicate the standard deviation of the strain field, as captured by DIC, in each specimen. Due to surface effects and porosity, the strain field on each specimen is not homogeneous. The elastic moduli are determined for the average strain

(box), and for the average strain plus/minus the standard deviation (error bars).

Figure 15 shows the yield strength (a), ultimate tensile strength (b), and elongation at break (c) for all build orientations and heat treatment conditions. The average strain of each specimen is considered when determining the respective properties. The average value of the reference specimens is indicated with the green line.

The tensile properties of the IN718 specimens manufactured by LPBF, averaged over all the build orientations, are shown in Table 8. For comparison, the values for the
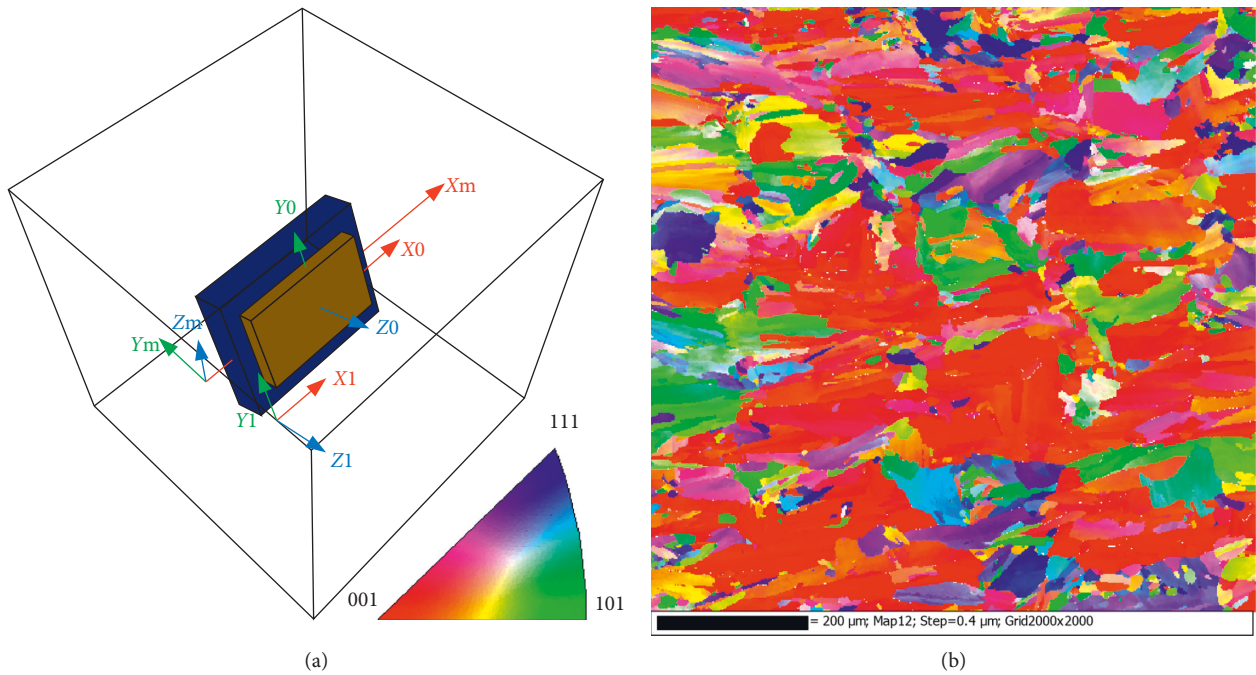
(a)

(b)

Figure 10: (a) Sample configuration and principal axes in the microscope chamber and (b) IPF-Y0 inverse pole figure grain map of the scanned area on the side wall of the sample oriented at 90° with respect to the build plate. The EBSD patterns were acquired with 0.4 μm step size.
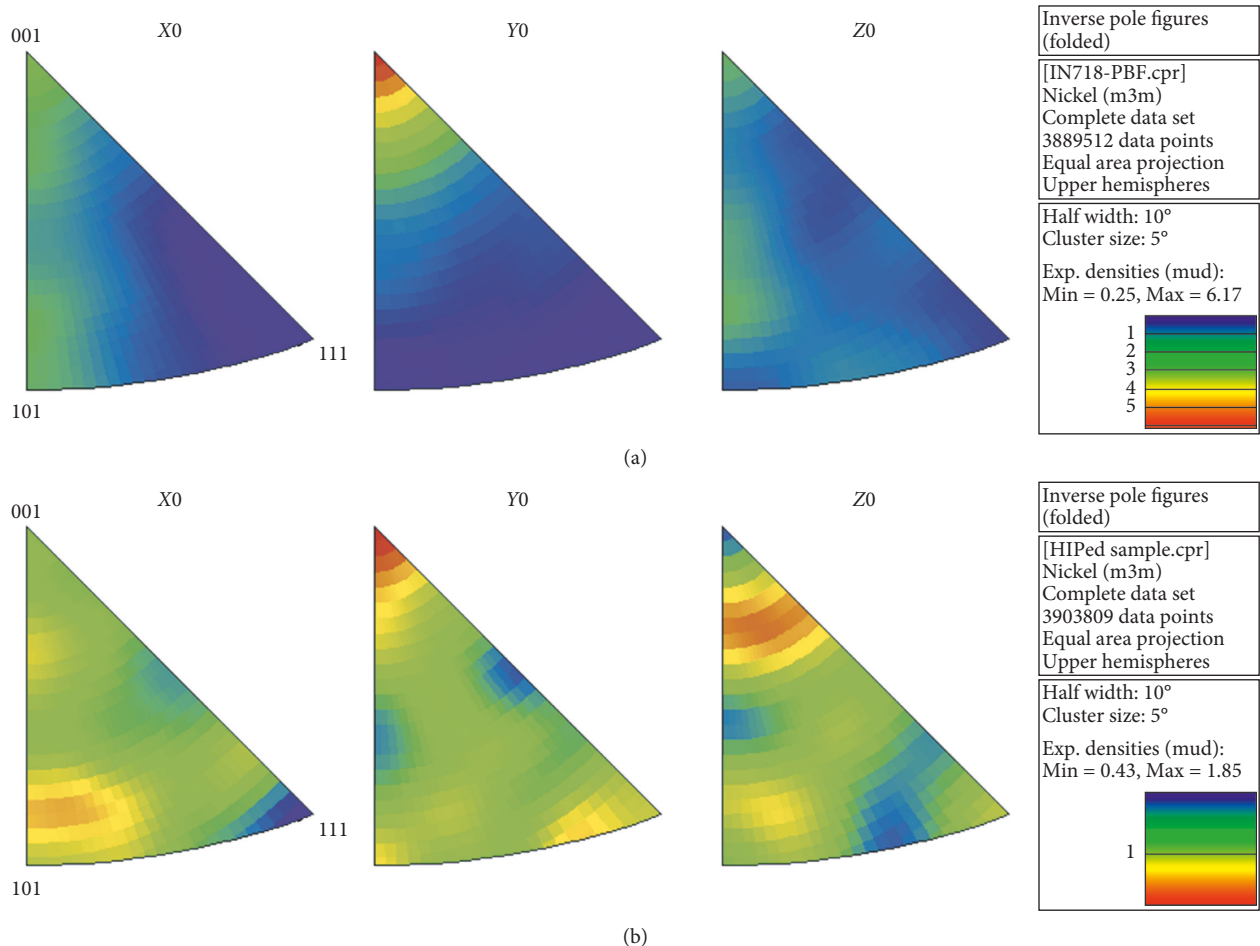

(a)

(b)

Figure 11: Inverse pole figure constructed based on 4 million data-points from the scanned area along the sample principal axes X0, Y0, and Z0 for (a) solution-treated and (b) HIP-treated sample.
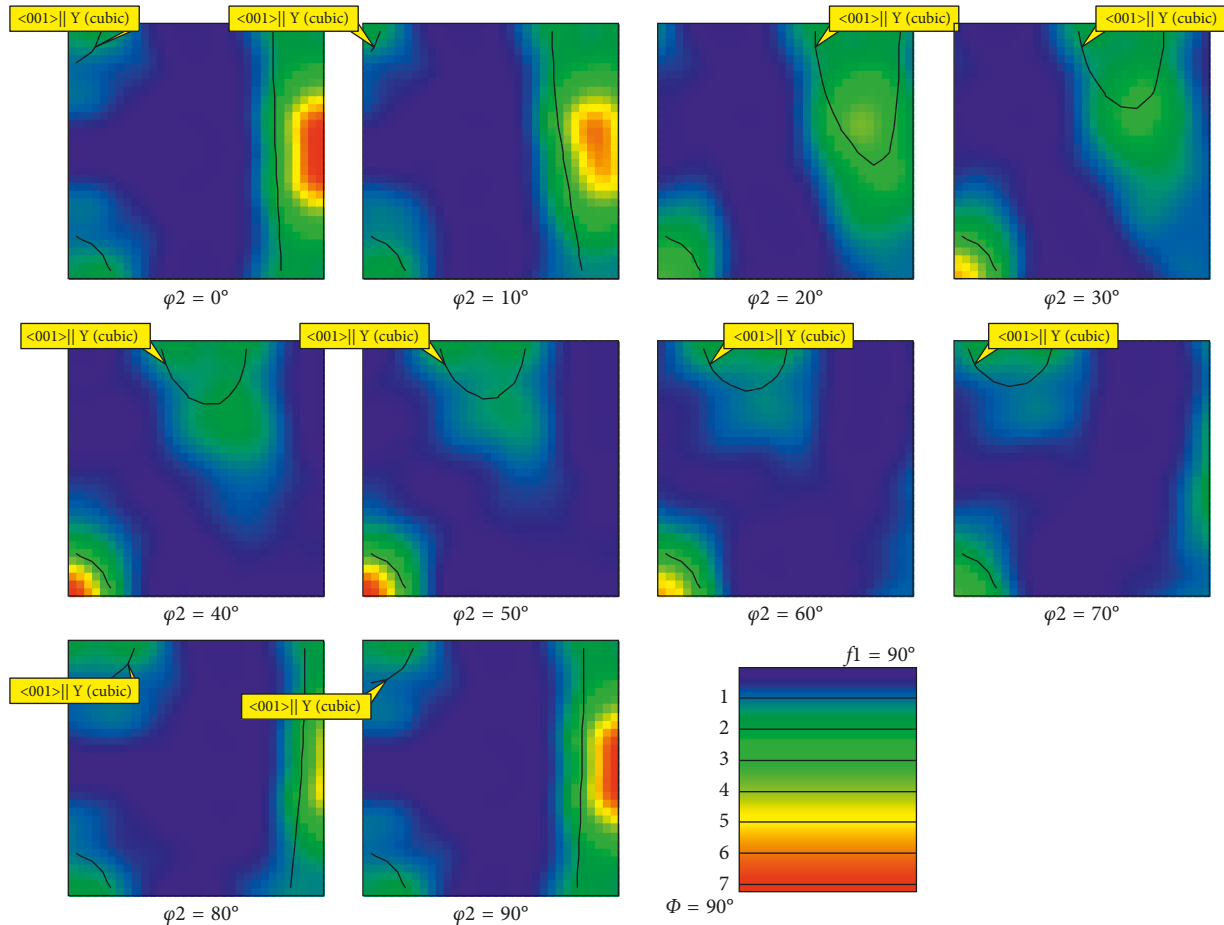
FIGURE 12: ODF sections of the scanned area. The boundaries of $<001>||Y0$ ideal texture components is shown with black solid line in different $\phi2$ sections.

reference specimens (machined from rolled and aged IN718) are included in parenthesis.

3.4. Elastic Constants.

The elastic constants, assuming transverse isotropy, acquired from the DIC strain fields are given in Table 9.

Table 10 shows the elastic constants obtained using the optimization algorithm described in Section 2.4 assuming transverse isotropy.

It is important to note that there are uncertainties associated with the calculated elastic constants. The elastic constants are determined from a calculated stress (Equation (7)), which is a function of the initial cross section area, the current transverse strain, and the applied force. The surface roughness is measured to be less than Ra = 1 μm for the 0° specimens, while peaking at the specimen oriented at 15° with Ra = 16 μm. The roughness then decreases to Ra = 5 μm as the specimens are raised towards 90°. HIP appears to reduce the surface roughness of the roughest surfaces by approximately 60%. The maximum uncertainty in the measurement of the initial cross section area due to the surface roughness is in the order of 80 μm^2, or 0.002% of the nominal cross section, introducing

negligible uncertainty. The standard deviation of the transverse strain has a much larger contribution to the uncertainty. The measured force is assumed to be accurate followed by load cell calibration certificate. The error of the calculated stress can be quantified by introducing the uncertainty of the initial cross-sectional area and the standard deviation of the transverse strain to Equation (7). The average error of the calculated stress is 0.57%, 0.19%, and 0.19% for set 1, set 2, and set 3, respectively. Due to the low error, only average values have been used to determine the elastic constants.

4. Discussion

The presented anisotropic material data, and the general methodology to obtain these, provide a basis for improved numerical modelling (finite element analysis) of the mechanical response of components produced by LPBF without postproduction machining. Even if machining is required for tolerances and surface finish, complex geometries with large inaccessible surface areas will remain the weakest link, and this justifies the method for obtaining the mechanical properties of the unmachined specimens as proposed in this study.
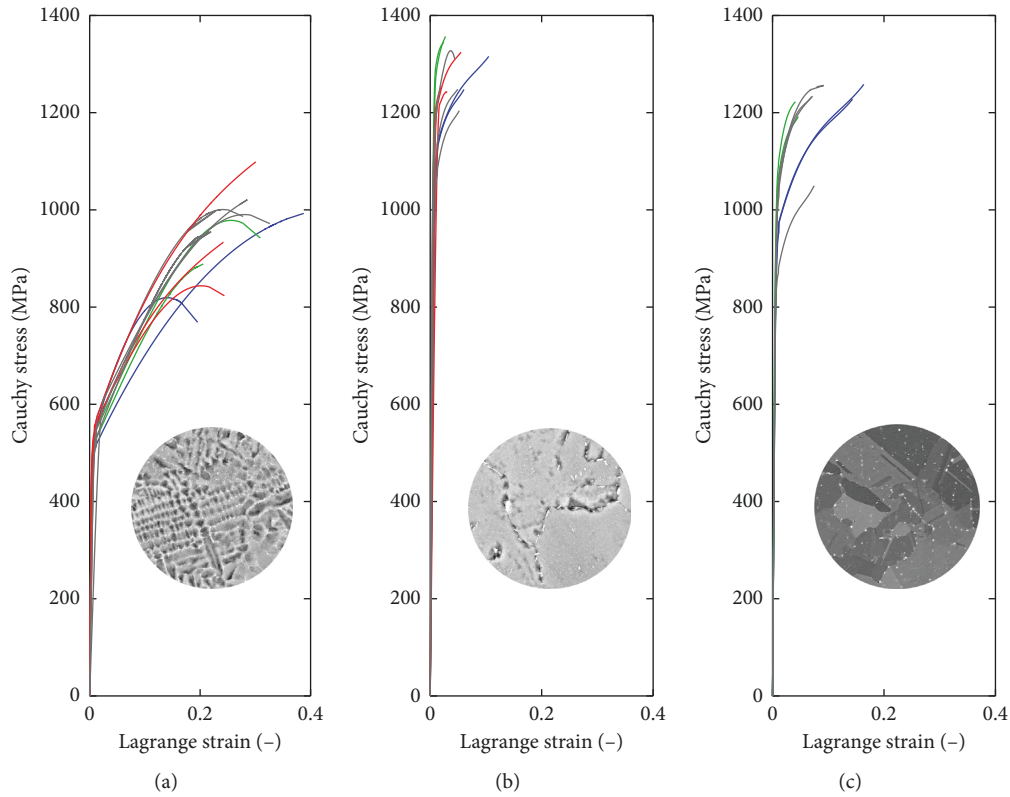
FIGURE 13: Cauchy stress plotted versus Lagrange strain for (a) S condition, (b) S + A condition, (c) S + H + A condition. Colours are according to Table 3.
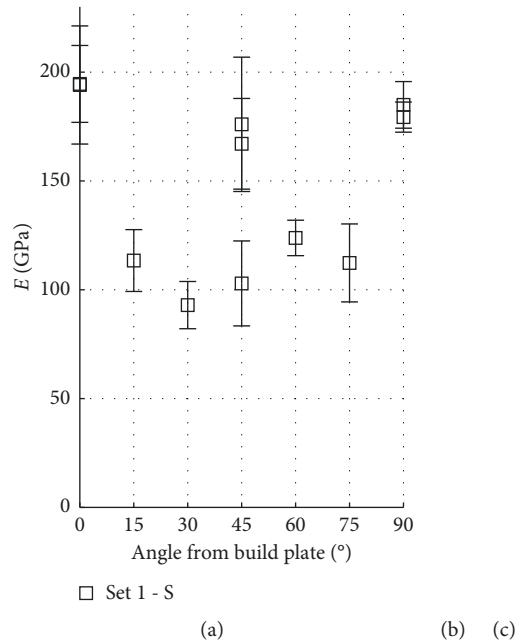

□ Set 1 - S

(a)   (b)   (c)

FIGURE 14: Mechanical properties of Set 1 (postprocessing "S"), Set 2 ("S + A"), and Set 3 ("S + H + A") with respect to orientation angle from build plate. Points indicate measured values (3 × 11 in each diagram), while the lines are either 2nd order polynomial fits (a), connecting lines (b and c) or least square fits (d), indicating the trend.

4.1. Powder, Laser, and Density Characteristics. Despite local inhomogeneities in the particle scale (Figure 6), the overall chemical composition of the powder is uniform. The presented defects in Figure 8(a), arising from metallurgical phenomena such as segregation or formation of eutectic phases, can possibly be related to local impurity enrichment
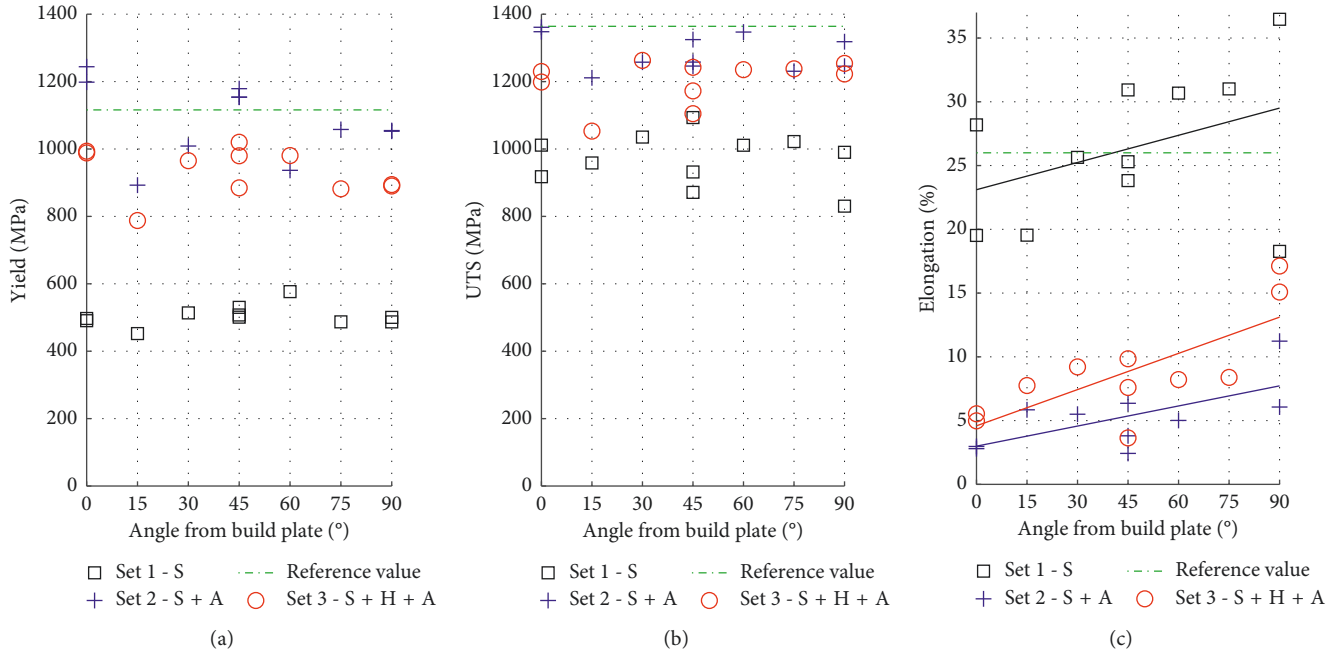
FIGURE 15: Yield strength (a), ultimate tensile strength (b), and elongation at break (c) of set 1, set 2, and set 3 with respect to orientation angle from build plate. Points indicate measured values while the lines in elongation indicate the least square fit.

TABLE 8: Average tensile properties for all eleven orientations. Values for the reference specimens (machined from rolled and aged IN718) are given in parenthesis.

	E (GPa)	UTS (MPa)	Yield stress (MPa)	Elongation at break (%)
SET 1	149 ± 40	970 ± 74	504 ± 30	26 ± 6
SET 2	181 ± 24 (193 ± 9)	1286 ± 52 (1364 ± 21)	1085 ± 106 (1116 ± 27)	5 ± 2 (26 ± 5)
SET 3	184 ± 30	1201 ± 63	933 ± 67	9 ± 4

TABLE 9: Elastic constants from DIC, for a transversely isotropic material model. This model is referred to as "DIC method" in figures below.

Elastic constants	Set 1 (S)	Set 2 (S + A)	Set 3 (S + H + A)
E_{xx} (GPa)	194	206	217
E_{zz} (GPa)	182	201	201
ν_{xy} (−)	0.4339	0.4748	0.4718
ν_{xz} (−)	0.4029	0.3650	0.4019
ν_{zx} (−)	0.3909	0.2045	0.2172
G_{xz} (GPa)	47	48	55
G_{xy} (GPa)	68	65	75

TABLE 10: Constants of optimized elastic model.

Elastic constants	Set 1 (S)	Set 2 (S + A)	Set 3 (S + H + A)
E_{xx} (GPa)	194	206	217
E_{zz} (GPa)	182	201	201
ν_{xy} (−)	0.3612	0.4994	0.3888
ν_{xz} (−)	0.3158	0.4999	0.4563
ν_{zx} (−)	0.3745	0.4877	0.4927
G_{xz} (GPa)	31	56	49
G_{xy} (GPa)	71	69	78

originating from non-IN718 powder particles. For instance, the presence of Al-rich particles (Figure 6) in the powder may result in anomalies and, therefore, proper cleaning of the build envelope, and powder-handling units play an important role in LPBF processing. Despite being recycled, the powder morphology and chemistry were well maintained (Figure 5), and the morphology measurements show no major deviations from the virgin powder specifications. The layer height after processing of the material decreased by 2–4% by comparing measured values in Table 7 with nominal values in Table 2. The source of such differences can be dependent on several parameters such as powder fusion and

densification, or shrinkage and dilution between each two adjacent layers [50]. On the one hand, a small difference between the measured and nominal values implies a relatively high packing ratio of the powder particles prior to fusion. On the other hand, it may also imply limited dilution between two adjacent layers. The latter case can be detrimental if low dilution leads to lack of fusion between the layers and cause formation of cracks. Lack of fusion was rarely found in the large areas being investigated, although Figure 8(a) proves the presence of such anomalies. In these cases, subsequent HIP will be required. Full closure of the crack will depend on the local chemistry, location and morphology of the anomaly, type of trapped gas inside cavities (pores), and the HIP parameters for that specific material. It is worth mentioning that

porosity in the powder particles may also play a central role in the evolution of postfusion porosity, since powder defects may retain throughout the entire process [51].

In this study, the energy per area (E_A) was 2.85 MJ/mm^2 (c.f. Table 2). Jia and Gu [52] achieved a relative density of 98.4% with an energy per area of 4.64 MJ/mm^2. Chlebus et al. [11] achieved a relative density in excess of 99.7% with an energy per area of 6.48 MJ/mm^2. According to the presented results in this work, high density can be achieved even with a low energy per area compared with the predecessor's applied parameters. Adjusting the process to build at high energy per area increases the baseline temperature and may cause the heat cycle to affect several layers below the last fusing surface. Depending on the peak temperature and the susceptibility of the material to form new phase constituents or anomalies, running the process at high temperature can be detrimental. Lower energy per area will confine the extent of the heat-affected zone (HAZ) in the previously fused layers.

4.2. Macro- and Microstructure. Beyond the effects of powder and part surface topography, the microstructure is also playing a significant role in determining the mechanical properties. Figures 8 and 9 show how the microstructure of a single alloy may change upon heat treatment. The grains are growing epitaxially throughout several layers before they are overgrown by other larger grains. The dendritic solidification pattern and $\gamma + \gamma''$ lamellae structure are visible in the microstructure. Observations of η and δ precipitates at the grain boundary were reported by several early researchers [42, 53, 54]. Their results unanimously propose that a small amount of these two phases may improve the notch sensitivity and resistance to intergranular crack propagation. The ageing of solution-treated IN718 is already showing these phases in the current study, and its indirect effect on the mechanical properties is shown in Figure 9(a). The benefit of HIP in eliminating anomalies was discussed earlier in Section 4.1. In addition to densification, the microstructure recrystallizes at high temperature during HIP, and the architecture of the grains and grain boundaries is largely affected [53–55]. According to Figure 9(b), the recrystallised grain boundaries transcend the primary γ grains, and subsequent ageing leads to the formation of precipitates not only on the recrystallised γ grains but also on the primary γ grains [26]. The presence of evenly distributed precipitates, even within the grains, seems to unitedly hamper the dislocation movements and causes a more uniform response of the material as can be seen when comparing set 1 with set 2 and set 3 in Figure 14(a).

In Figure 10(b), it was also illustrated that LPBF is a directional processing route that influences the grain structure, the grain morphology, and the crystallographic texture of the material. Preferred alignment of <100> along the build direction may weaken the material if it is built at an angle. The curvilinear heat flow vector argument is shown to be the dominant growth mechanism for high and low cooling kinetics [39]. The evolution of <100> along the build direction is primarily due to low layer thickness that embodies fewer grains within each layer, and high processing

speed (i.e., laser scanning speed), which determines the range of grain growth kinetics. In such conditions, unlike welding, for example, the grains are not given sufficient time to bend behind the heat source (see e.g., Figure 2(a)).

4.3. Mechanical Properties. Consider the stress-strain curves presented in Figure 13. Ageing (Figures 13(b) and 13(c)) increases the yield stress and ultimate tensile strength at the expense of elongation, compared with the nonaged specimens in Figure 13(a). HIP before ageing will somewhat reduce the yield strength and ultimate tensile strength and increase the elongation (Figures 13(b) and 13(c)).

Figure 14 shows the elastic moduli for all three sets as function of the specimens' build angle relative to the build platform. For set 1, the elastic modulus is highest for the specimen built at 0° with respect to the build plate. It then drops as the specimens are raised towards 45°. The elastic modulus then increases as the angle is raised further up to 90°. The three measured values for the specimens at 45° are 167 ± 20.8 GPa, 103 ± 19.5 GPa, and 176 ± 30.1 GPa, for orientations XZ-45B, XY + 45B, and YZ + 45A, respectively. A possible explanation of the large variation in the 45° data is given in Section 4.4. As can be seen in Figure 14, ageing will increase the modulus of the material significantly. The average modulus is 149 ± 40 GPa, 181 ± 24 GPa, and 184 ± 30 GPa for set 1, set 2, and set 3, respectively.

Recall that the microstructure in set 1 primarily consists of FCC γ-phase with slip system $\{111\} <1\bar{1}0>$, and that the material exhibits a strong {100} fibre texture (Figures 11 and 12). Consider, for arguments sake, the material as single crystal FCC. The elastic modulus in any particular crystallographic direction can then be calculated using the following equation [56]:

$$\frac{1}{E_{[hkl]}} = \frac{1}{E_{<100>}} - 3\left(\frac{1}{E_{<100>}} - \frac{1}{E_{<111>}}\right)(\alpha^2\beta^2 + \alpha^2\gamma^2 + \beta^2\gamma^2), \tag{10}$$

where $E_{<100>}$ and $E_{<111>}$ are the moduli in the <100> and <111> directions, respectively, and α, β, and γ describe a unit vector $\mathbf{v} = [\alpha\ \beta\ \gamma]$ within the crystallographic plane of interest where α, β, and γ are the direction cosines with respect to [100], [010], and [001]. In the current study, we are interested in the modulus in the {100} plane under different loading angles. The inset in Figure 16 shows the {100} plane in a cubic system with the unit vector $\mathbf{v} = [0\cos(\theta)\sin(\theta)]$, and the blue line (Equation (10)) shows the moduli under different load angles with values for $E_{<100>}$ being greater than $E_{<111>}$ as measured with DIC for set 1. The calculated modulus in Figure 16 compares well with the observed behaviour of the material as seen in Figure 14(a).

Figure 15(a) shows the yield stress for all specimens as a function of build angle. For set 1, the yield stress is at its maximum at a 60° angle to the build plate. Although the sample size for set 1 is small, and thus not statistically significant, crystallographic theory supports the observed
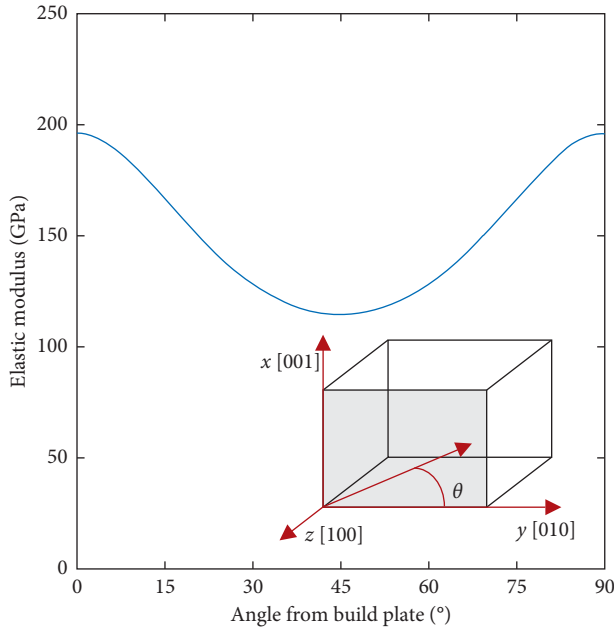
FIGURE 16: Elastic modulus is according to Equation (10) with a value for $E_{<100>} > E_{<111>}$ as measured with DIC for set 1. Inset: {100} plane in a FCC crystal with *xyz* and corresponding (hkl) coordinates.

FIGURE 17: Yield stress for set 1 compared with the inverse Schmid factor for set 1.

maxima close to the theoretical maxima at 54°, as will be shown in the next paragraph. In the aged and HIP + aged condition, the scatter in the data is large and no clear anisotropic trends are observed. However, it is clear that the average yield stress increases as the material is aged, and HIP before ageing reduces the average yield stress somewhat.

Consider again the material as single-crystal FCC. The Schmid factor can then be employed to describe the anisotropic behaviour with respect to build angle, as previously done by Ni et al. [32], for the same material and process as in the present study. The yield stress can be expressed as

$$\sigma_{\text{yield}} \geq \frac{\tau_c}{\cos(\phi)\cos(\beta)}, \tag{11}$$

where τ_c is the critical resolved shear stress in slip systems, φ is the angle between the axial load and the normal direction of the slip plane, and β is the angle between the axial load and the slip direction. The term $\cos(\phi)\cos(\beta)$ is known as the Schmid factor. With the current slip system φ and β sum to 90° and the Schmid factor can be expressed as $(1/2)\sin(2\phi)$. For set 1, the yield stress and the inverse of the Schmid factor are plotted as function of build angle in Figure 17. The error bars represent the standard deviation of the strain field for each specimen. The general trend for the inverse Schmid factor and the yield stress is the same. If the material did not exhibit the strong texture observed in this study, Taylor's factor may be employed to estimate the deformation instead of the Schmid factor. However, with the texture exhibited in the present material the Taylor factor and the Schmid factor will be comparable.
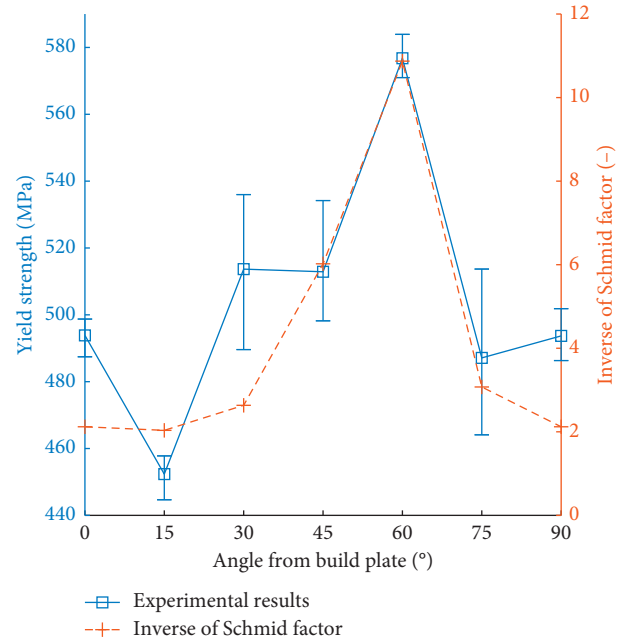
The trend of the yield strength of set 1 corresponds with the Schmid factor, as shown in Figure 17, with a minimum in yield strength at a 15° angle from the build plate and a maximum yield strength at a 60° angle from the build plate. This trend is not observed for set 2 and set 3.

After ageing, and after HIP and ageing, the average yield stress increases to 1085 ± 106 MPa and 933 ± 67 MPa, respectively. The precipitation hardening that occurs during ageing will increase the yield stress due to the pinning of grain boundaries and the stopping of dislocation movement. The standard deviation of the yield stress is reduced when HIP is done prior to ageing, indicating a homogenization effect. The magnitude of the yield stress is also slightly reduced when HIP is done before ageing, most likely due to recrystallization and evolution of twin grain boundaries.

Figures 15 and 14(b) show the ultimate tensile strength for the three different heat treatment sets as function of build angle. Again, it is obvious that ageing increases the materials strength. The ultimate tensile strength in set 1 is significantly lower compared with the aged variants. It is observed that the ultimate tensile strength is lower when the material has undergone HIP processing, as was the case for yield stress. Further analysis of ultimate tensile strength is considered unnecessary for this material as its main application is in aerospace where plastic deformation would be considered as failure.

Figure 15(c) shows the elongation at break for the three different heat treatment sets as function of build angle. The average elongation at break for set 1 is 26 ± 5%, with increasing elongation at break as the build angle increases. The same trend is observed for the heat-treated samples, but the magnitude of the elongation at break is greatly reduced. The

elongation at break for set 3 (S + H + A) is higher compared with the elongation at break for set 2 (S + A). This is attributed to a reduction in the residual stresses and hardness of the precipitates after HIP.

The angle between the axial load and the material texture will determine the failure mode. For the tensile specimens with main loading axis in the build plate plane (0°), the columnar grains are perpendicular to the loading direction (c.f. growth mechanisms in Section 1.3), promoting mode I type failure. For the specimens with main axis along the perpendicular to the build plate (90° build angle), the columnar grains are in general parallel to the load direction. This will limit the possibility of mode I failure. The lowest elongation at break should then be observed for the 0° specimens and increase gradually to a maximum for the 90° specimens. This hypothesis is supported by the data seen in Figure 15(c).

Consider the average mechanical properties for all orientations in Table 8. The results for the aged specimens (set 2) compare well with those of the reference specimens (machined from rolled and aged IN718). The specimens of set 2 have average modulus, yield stress, and UTS that are 94%, 94%, and 97% of the reference's values, respectively. However, the elongation at break is significantly higher for the reference specimens than for the set 2 specimens.

4.4. Elastic Constants. The elastic constants given in Tables 9 and 10 can be used in FE analysis (e.g., Abaqus) directly to predict the anisotropic elastic behaviour of a general three-dimensional part with a certain build orientation. Next, the model is discussed and verified by performing simulations with load conditions simulating the physical experiments. The first approach of determining the elastic constants, based on direct DIC measurements, is referred to as the "DIC method," while the approach employing the optimization algorithm is referred to as the "optimized method."

Figure 18 shows the elastic modulus numerically determined with the DIC method and the optimized method, compared with the experimental results for each heat treatment condition (sets 1, 2, and 3). When using the DIC method, the elastic modulus follows a 4th order polynomial as discussed in the previous section (Equation (10) with $E(0°) > E(90°) > E(45°)$). The same trend is observed with the optimized method, which follows the experimentally determined data more closely. This is a result of how the optimization algorithm treats each individual stress/strain pair equally, and thus the high values at 45° are given less weight.

The experimentally determined elastic moduli deviate from the calculated moduli, with higher modulus for the 45° angle, particularly for the two specimens with orientation *XZ*-45B and *YZ* + 45A, which are not simply rotated from a "flat" orientation such as *XY* + 45B (Figure 4 and Table 3). For the orientations *XZ*-45B and *YZ* + 45A, the projection of the specimen cross section along the *Z* axis (of the build chamber) is $w/\cos(45°)$, where w is the width of the sample (2.5 mm in the gauge section). On the other hand, for the orientation *XY* + 45B, the projection of the specimen cross section along the *Z* axis is $t/\cos(45°)$, where t is the thickness of the sample (1.5 mm). When loading specimens with 45° build angle, the grain boundaries will either align with the slip line and cause de-cohesion, or twin subgrains will form, which will introduce twinning-induced plasticity [57]. The experimental results shown in Figure 18(a) might indicate that for the orientations *XZ*-45B and *YZ* + 45A, subgrains are formed, while for *XY* + 45B, the grains align with the slip line and the plasticity is higher. Chlebus et al. [11] reported values for moduli in the solution treated only condition (set 1) with the trend E $(45)° > E(0°) > E(90°)$, which is in line with activation of slip lines under loading. Considering the magnitude of the moduli for specimens oriented at angles 15°, 30°, 60°, and 75° in the present study, the data suggest the worst-case scenario should be assumed, where the grains align with the slip line. This will in turn give a more conservative model. There are also significant differences between the study by Chlebus et al. and the present study when it comes to laser parameters, alloy composition, and heat treatment procedures. The spread in the $E(45°)$ data is far larger than the spread in the data for $E(0°)$ and $E(90°)$ for all three sets, which indicates that some competing effect—like the one described in this paragraph—might be the source of the presented disparity.

Using the DIC method, the modulus is calculated to be higher than the experimental values for 15°, 30°, 60°, and 75°, resulting in a possibility to overestimate the stiffness in components with walls, etc. oriented in this range of angles.

Both the DIC method and the optimized method predict moduli higher than the observed values for 15°, 30°, 60°, and 75°, with the exception of set 2 at 30° and set 3 at 30° and 60°. However, the optimized method is not as strongly influenced by the apparent outliers at 15°, 60°, and 75° compared with the DIC method. This in turn suggests that the optimized method is less vulnerable to noise in the data. For all heat treatment conditions, the optimized method gives a more conservative estimate of the moduli.

5. Conclusions

(i) A method has been demonstrated for obtaining anisotropic (transverse isotropic) elastic constants for material processed by laser powder bed fusion (LPBF). The method is based on building a set of tensile specimens, oriented in a systematic manner on the build plate, and using digital image correlation (DIC) during the tensile tests. The current study is focused on the response of nonmachined specimens, inspired by the fact that in complicated AM geometries, postmachining may be difficult or even impossible.

(ii) Extensive tensile testing of a single specimen geometry built with different orientations shows that the LPBF process induces mechanical anisotropy.
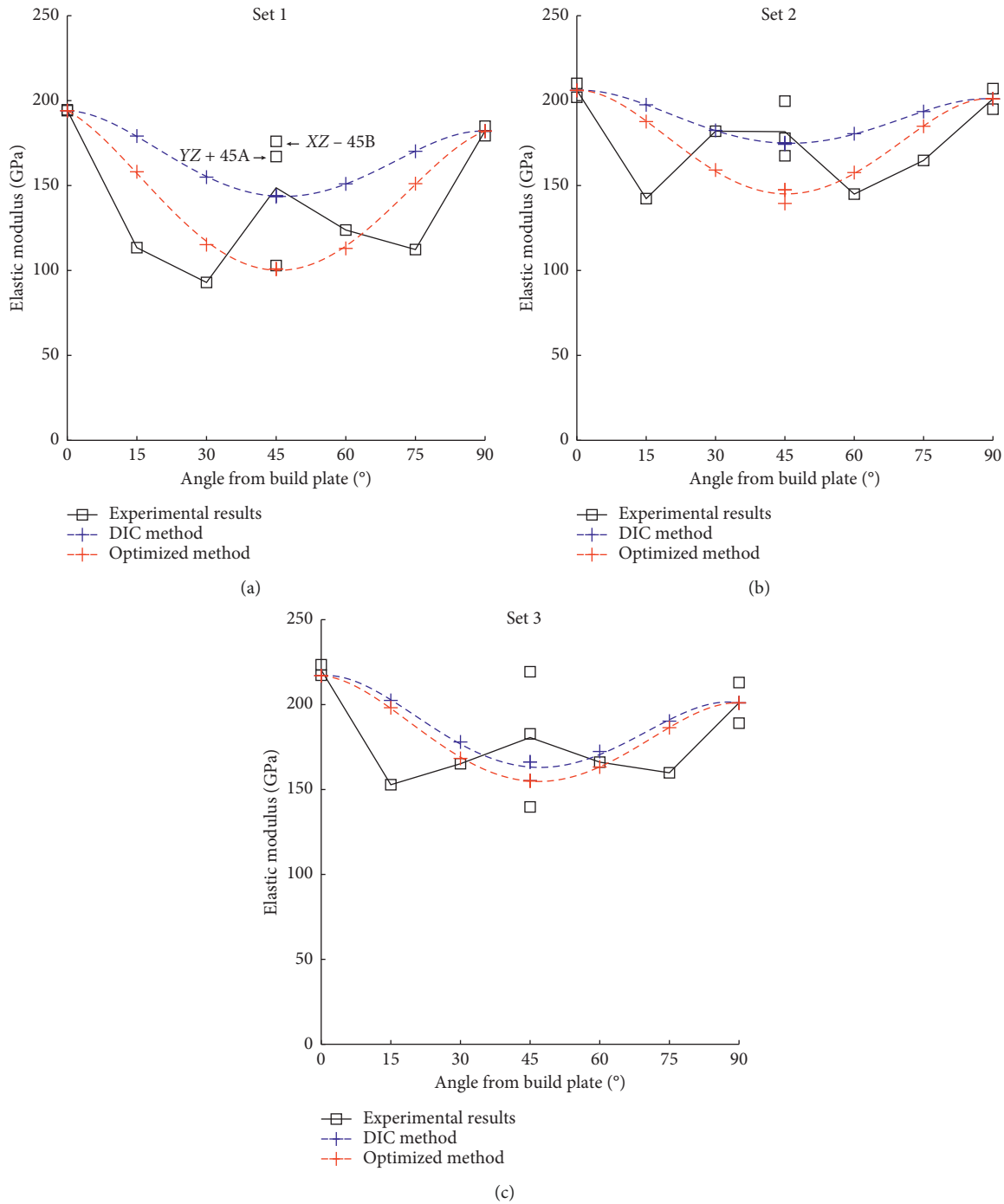
(a)

(b)

(c)

FIGURE 18: Elastic modulus in the load direction as measured directly, calculated based on the DIC measurements, and calculated based on the optimized elastic model for (a) as built condition, (b) aged condition, and (c) HIP + aged condition.

Therefore, care should be taken when orienting components in the build chamber to maximize the mechanical properties.

(iii) Two approaches for determining the anisotropic elastic constants are presented in this study. In the future, more experimental data will be included to consolidate the reliability and robustness of the determined elastic constants.

(iv) While all the tensile properties are influenced by the build angle of the test specimen relative to the build plate, the elastic modulus and the elongation at break show the highest dependence on build angle.

(v) Ageing has a large effect on the mechanical properties; it improves the elastic modulus, yield stress, and ultimate tensile strength, but reduces the elongation at break. Hot isostatic pressing (HIP)

before ageing increases the elongation at break at the expense of a reduction in elastic modulus, yield stress, and ultimate tensile strength. Furthermore, HIP does not reduce the scatter in mechanical properties among the tested samples, and evidence of the initial structure and texture is still apparent.

(vi) This study confirms that LPBF processing of IN718 introduces texture, and the variation in mechanical properties can be explained by crystallographic theories such as Schmid's theory.

Data Availability

The raw data required to reproduce these findings cannot be shared at this time as the data also form part of an ongoing study. The processed data required to reproduce these findings cannot be shared at this time as the data also form part of an ongoing study.

Conflicts of Interest

The authors declare that there are no conflicts of interest regarding the publication of this paper.

Authors' Contributions

The authors Even W. Hovig and Amin S. Azar contributed equally to this work.

Acknowledgments

References

[1] B. E. Carroll, T. A. Palmer, and A. M. Beese, "Anisotropic tensile behavior of Ti–6Al–4V components fabricated with directed energy deposition additive manufacturing," *Acta Materialia*, vol. 87, pp. 309–320, 2015.

[2] W. E. Luecke and J. A. Slotwinski, "Mechanical properties of austenitic stainless steel made by additive manufacturing," *Journal of research of the National Institute of Standards and Technology*, vol. 119, p. 398, 2014.

[3] T. Wang, Y. Zhu, S. Zhang, H. Tang, and H. Wang, "Grain morphology evolution behavior of titanium alloy components during laser melting deposition additive manufacturing," *Journal of Alloys and Compounds*, vol. 632, pp. 505–513, 2015.

[4] J. J. Lewandowski and M. Seifi, "Metal additive manufacturing: a review of mechanical properties," *Annual Review of Materials Research*, vol. 46, no. 1, pp. 151–186, 2016.

[5] L. Thijs, M. L. M. Sistiaga, R. Wauthle, Q. Xie, J.-P. Kruth, and J. Van Humbeeck, "Strong morphological and crystallographic texture and resulting yield strength anisotropy in selective laser melted tantalum," *Acta Materialia*, vol. 61, no. 12, pp. 4657–4668, 2013.

[6] F. List, R. R. Dehoff, L. E. Lowe, and W. J. Sames, "Properties of Inconel 625 mesh structures grown by electron beam additive manufacturing," *Materials Science and Engineering: A*, vol. 615, pp. 191–197, 2014.

[7] N. Gardan and A. Schneider, "Topological optimization of internal patterns and support in additive manufacturing," *Journal of Manufacturing Systems*, vol. 37, pp. 417–425, 2015.

[8] C. C. Swan and I. Kosaka, "Voigt-Reuss topology optimization for structures with nonlinear material behaviors," *International Journal for Numerical Methods in Engineering*, vol. 40, no. 20, pp. 3785–3814, 1997.

[9] B. Vrancken, L. Thijs, J.-P. Kruth, and J. Van Humbeeck, "Heat treatment of Ti6Al4V produced by selective laser melting: microstructure and mechanical properties," *Journal of Alloys and Compounds*, vol. 541, pp. 177–185, 2012.

[10] T. Vilaro, C. Colin, and J.-D. Bartout, "As-fabricated and heat-treated microstructures of the Ti-6Al-4V alloy processed by selective laser melting," *Metallurgical and Materials Transactions A*, vol. 42, no. 10, pp. 3190–3199, 2011.

[11] E. Chlebus, K. Gruber, B. Kuźnicka, J. Kurzac, and T. Kurzynowski, "Effect of heat treatment on the microstructure and mechanical properties of Inconel 718 processed by selective laser melting," *Materials Science and Engineering: A*, vol. 639, pp. 647–655, 2015.

[12] T. Trosch, J. Strößner, R. Völkl, and U. Glatzel, "Microstructure and mechanical properties of selective laser melted Inconel 718 compared to forging and casting," *Materials Letters*, vol. 164, pp. 428–431, 2016.

[13] D. Tomus, Y. Tian, P. A. Rometsch, M. Heilmaier, and X. Wu, "Influence of post heat treatments on anisotropy of mechanical behaviour and microstructure of Hastelloy-X parts produced by selective laser melting," *Materials Science and Engineering: A*, vol. 667, pp. 42–53, 2016.

[14] T. C. T. Ting, *Anisotropic Elasticity: Theory and Applications*, Oxford University Press, New York, NY, USA, 1996.

[15] E. V. Morozov and V. V. Vasiliev, "Determination of the shear modulus of orthotropic materials from off-axis tension tests," *Composite Structures*, vol. 62, no. 3-4, pp. 379–382, 2003.

[16] J. C. Lippold, S. D. Kiser, and J. N. DuPont, *Welding Metallurgy and Weldability of Nickel-Base Alloys*, John Wiley and Sons, Hoboken, NJ, USA, 2011.

[17] R. Cozar and A. Pineau, "Morphology of γ'and γ" precipitates and thermal stability of inconel 718 type alloys," *Metallurgical Transactions*, vol. 4, no. 1, pp. 47–59, 1973.

[18] S. Singh Handa, J. Andersson, and M. Eynian, *Precipitation of carbides in a Ni-based superalloy*, Ph.D. thesis, Department of Engineering Science, University West, Trollhättan, Sweden, 2014.

[19] N. Saunders, Z. Guo, X. Li, A. Miodownik, and J.-P. Schille, "Modelling the material properties and behaviour of Ni-based superalloys," in *Proceedings of the 10th International Symposium on Superalloys*, pp. 849–858, Champion, PA, USA, September 2004.

[20] A. Oradei-Basile and J. F. Radavich, "A current TTT diagram for wrought alloy 718," in *Proceedings of Superalloys 718, 625 and Various Derivatives*, pp. 325–335, Pittsburgh, PA, USA, June 1991.

[21] A. Simchi, "Direct laser sintering of metal powders: mechanism, kinetics and microstructural features," *Materials Science and Engineering: A*, vol. 428, no. 1, pp. 148–158, 2006.

[22] M. E. Aydinöz, F. Brenne, M. Schaper et al., "On the microstructural and mechanical properties of post-treated additively manufactured Inconel 718 superalloy under quasistatic and cyclic loading," *Materials Science and Engineering A*, vol. 669, pp. 246–258, 2016.

[23] D. L. Bourell, H. L. Marcus, J. W. Barlow, and J. J. Beaman, "Selective laser sintering of metals and ceramics," *International Journal of Powder Metallurgy*, vol. 28, no. 4, pp. 369–381, 1992.

[24] M. Dressler, M. Röllig, M. Schmidt, A. Maturilli, and J. Helbert, "Temperature distribution in powder beds during 3D printing," *Rapid Prototyping Journal*, vol. 16, no. 5, pp. 328–336, 2010.

[25] D. H. Smith, J. Bicknell, L. Jorgensen et al., "Microstructure and mechanical behavior of direct metal laser sintered Inconel alloy 718," *Materials Characterization*, vol. 113, pp. 1–9, 2016.

[26] K. Amato, S. Gaytan, L. Murr et al., "Microstructures and mechanical behavior of Inconel 718 fabricated by selective laser melting," *Acta Materialia*, vol. 60, no. 5, pp. 2229–2239, 2012.

[27] X. Zhao, J. Chen, X. Lin, and W. Huang, "Study on microstructure and mechanical properties of laser rapid forming Inconel 718," *Materials Science and Engineering: A*, vol. 478, no. 1-2, pp. 119–124, 2008.

[28] F. Liu, X. Lin, C. Huang et al., "The effect of laser scanning path on microstructures and mechanical properties of laser solid formed nickel-base superalloy Inconel 718," *Journal of Alloys and Compounds*, vol. 509, no. 13, pp. 4505–4509, 2011.

[29] A. Simchi and H. Pohl, "Effects of laser sintering processing parameters on the microstructure and densification of iron powder," *Materials Science and Engineering: A*, vol. 359, no. 1-2, pp. 119–128, 2003.

[30] B. N. Turner and S. A. Gold, "A review of melt extrusion additive manufacturing processes: II. Materials, dimensional accuracy, and surface roughness," *Rapid Prototyping Journal*, vol. 21, no. 3, pp. 250–261, 2015.

[31] W. E. Frazier, "Metal additive manufacturing: a review," *Journal of Materials Engineering and Performance*, vol. 23, no. 6, pp. 1917–1928, 2014.

[32] M. Ni, C. Chen, X. Wang et al., "Anisotropic tensile behavior of in situ precipitation strengthened Inconel 718 fabricated by additive manufacturing," *Materials Science and Engineering: A*, vol. 701, pp. 344–351, 2017.

[33] O. Scott-Emuakpor, T. George, C. Holycross, J. Bruns, and A. Zearley, "Bending fatigue life comparison between DMLS and cold-rolled nickel alloy 718," in *Proceedings of the Prognostics and Health Management Solutions Conference (MFPT 2014)*, Virginia Beach, VA, USA, May 2014.

[34] M. M. Kirka, D. Greeley, C. Hawkins, and R. Dehoff, "Effect of anisotropy and texture on the low cycle fatigue behavior of Inconel 718 processed via electron beam melting," *International Journal of Fatigue*, vol. 105, pp. 235–243, 2017.

[35] V. Badiru Vhance and D. A. B. Liu, *Valencia, Additive Manufacturing Handbook: Product Development for the Defense Industry*, CRC Press Inc., Boca Raton, FL, USA, 2017.

[36] J.-P. Choi, G.-H. Shin, S. Yang et al., "Densification and microstructural investigation of Inconel 718 parts fabricated by selective laser melting," *Powder Technology*, vol. 310, pp. 60–66, 2017.

[37] X. Wang, T. Keya, and K. Chou, "Build height effect on the Inconel 718 parts fabricated by selective laser melting," *Procedia Manufacturing*, vol. 5, pp. 1006–1017, 2016.

[38] A. Keshavarzkermani, M. Sadowski, and L. Ladani, "Direct metal laser melting of Inconel 718: process impact on grain formation and orientation," *Journal of Alloys and Compounds*, vol. 736, pp. 297–305, 2018.

[39] A. S. Azar, E. Østby, and O. M. Akselsen, "Effect of hyperbaric chamber gas on transformation texture of the API-X70 pipeline weld metal," *Metallurgical and Materials Transactions A*, vol. 43, no. 9, pp. 3162–3178, 2012.

[40] L. Murr, S. Li, Y. Tian, K. Amato, E. Martinez, and F. Medina, "Open-cellular Co-base and Ni-base superalloys fabricated by electron beam melting," *Materials*, vol. 4, no. 4, pp. 782–790, 2011.

[41] L. E. Murr, E. Martinez, S. Gaytan et al., "Microstructural architecture, microstructures, and mechanical properties for a nickel-base superalloy fabricated by electron beam melting," *Metallurgical and Materials Transactions A*, vol. 42, no. 11, pp. 3491–3508, 2011.

[42] X. Wang, X. Gong, and K. Chou, "Review on powder-bed laser additive manufacturing of Inconel 718 parts," in *Proceedings of ASME 2015 International Manufacturing Science and Engineering Conference*, p. V001T02A063, American Society of Mechanical Engineers, Charlotte, NC, USA, 2015.

[43] SLM Solutions, "3D METALS, discover the variety of metal powders," October 2018, https://slm-solutions.com/sites/default/files/downloads/201en171023-01-001-powder_web.pdf.

[44] D. D. Gu, W. Meiners, K. Wissenbach, and R. Poprawe, "Laser additive manufacturing of metallic components: materials, processes and mechanisms," *International Materials Reviews*, vol. 57, no. 3, pp. 133–164, 2012.

[45] S. Ernst, "Postweld heat treatment of nonferrous high-temperature materials," in *ASM Handbook*, vol. 6, pp. 572–574, ASM International, Geauga County, OH, USA, 1993.

[46] F. Grytten, H. Daiyan, M. Polanco-Loria, and S. Dumoulin, "Use of digital image correlation to measure large-strain tensile properties of ductile thermoplastics," *Polymer Testing*, vol. 28, no. 6, pp. 653–660, 2009.

[47] R. Miller, A. Kolipaka, M. P. Nash, and A. A. Young, "Estimation of transversely isotropic material properties from magnetic resonance elastography using the optimised virtual fields method," *International Journal for Numerical Methods in Biomedical Engineering*, vol. 34, no. 6, article e2979, 2018.

[48] J. J. Vlassak and W. D. Nix, "Measuring the elastic properties of anisotropic materials by means of indentation experiments," *Journal of the Mechanics and Physics of Solids*, vol. 42, no. 8, pp. 1223–1245, 1994.

[49] A. Vogel, S. Diplas, A. Durant et al., "Reference dataset of volcanic ash physicochemical and optical properties," *Journal of Geophysical Research: Atmospheres*, vol. 122, no. 17, pp. 9485–9514, 2017.

[50] V. Gunenthiram, P. Peyre, M. Schneider, M. Dal, F. Coste, and R. Fabbro, "Analysis of laser–melt pool–powder bed interaction during the selective laser melting of a stainless steel," *Journal of Laser Applications*, vol. 29, no. 2, article 022303, 2017.

[51] M. Zhang, C.-N. Sun, X. Zhang et al., "Fatigue and fracture behaviour of laser powder bed fusion stainless steel 316L: influence of processing parameters," *Materials Science and Engineering: A*, vol. 703, pp. 251–261, 2017.

[52] Q. Jia and D. Gu, "Selective laser melting additive manufacturing of Inconel 718 superalloy parts: densification, microstructure and properties," *Journal of Alloys and Compounds*, vol. 585, pp. 713–721, 2014.

[53] A. Casanova, N. Martín-Piris, M. Hardy, and C. Rae, "Evolution of secondary phases in alloy ATI 718Plus® during processing," *MATEC Web of Conferences*, vol. 14, article 09003, 2014.

[54] E. McDevitt, S. Oppenheimer, R. Kearsey, and J. Tsang, *Crack Growth Behavior in ATI 718Plus® Alloy, Materials Science Forum*, Trans Tech Publications, Zürich, Switzerland, 2012.

[55] X. Wang, X. Gong, and K. Chou, "Review on powder-bed laser additive manufacturing of Inconel 718 parts," *Proceedings of the Institution of Mechanical Engineers, Part B: Journal of Engineering Manufacture*, vol. 231, no. 11, pp. 1890–1903, 2017.

[56] K. M. Knowles and P. R. Howie, "The directional dependence of elastic stiffness and compliance shear coefficients and shear moduli in cubic materials," *Journal of Elasticity*, vol. 120, no. 1, pp. 87–108, 2014.

[57] J. Jung, J. I. Yoon, J. G. Kim, M. I. Latypov, J. Y. Kim, and H. S. Kim, "Continuum understanding of twin formation near grain boundaries of FCC metals with low stacking fault energy," *NPJ Computational Materials*, vol. 3, no. 1, p. 21, 2017.

The Scientific World Journal

Journal of Applied Chemistry

Journal of Nanomaterials

Scientifica

International Journal of Polymer Science

Advances in Chemistry

Advances in Physical Chemistry

International Journal of Analytical Chemistry

Hindawi

Submit your manuscripts at
www.hindawi.com

Advances in Condensed Matter Physics

Journal of Chemistry

International Journal of Biomaterials

Advances in High Energy Physics

Journal of Engineering

Journal of Nanotechnology

International Journal of Corrosion

Journal of Materials

BioMed Research International

Advances in Tribology

Advances in Materials Science and Engineering